JOURNAL OF AIRCRAFT
Vol. 34, No. 3, May–June 1997

Refined Aeroelastic Analysis of Hingeless Rotor Blades in Hover

Maeng Hyo Cho,* Seong Min Jeon,† Sung Hyun Woo,‡ and In Lee§
Korea Advanced Institute of Science and Technology, Taejon 305-701, Republic of Korea

The aeroelastic response and stability of hingeless rotor blades in hover are investigated using both refined structural and aerodynamic models. Finite elements based on a large deflection-type beam theory are used for structural analysis. Although the strain components in the beam element are assumed to be small compared to unity, no kinematical limitations are imposed on the magnitude of displacements and rotations. A three-dimensional aerodynamic model including compressibility effect, which is a thin lifting-surface theory based on the unsteady vortex lattice method, is applied to evaluate the aerodynamic loads. A thin lifting-surface and its wake are represented by a number of the quadrilateral vortex-ring elements. The wake geometry is prescribed from the known generalized equations. Numerical results of the steady-state deflections and the stability for the stiff in-plane rotor blade are presented. It is found that the three-dimensional aerodynamic tip-relief, unsteady wake dynamics, and compressibility effects, not predicted in the two-dimensional strip theory, play an important role in the hingeless rotor aeroelastic analysis in hover.

Nomenclature

A = aerodynamic influence coefficient matrix
a_0 = two-dimensional lift-curve slope
C_p = pressure coefficient
c = blade chord length
c_{d_0} = profile drag coefficient
dC_T/dr = spanwise thrust loading, thrust/$\rho_a \pi R(\Omega R)^2$
$G(\boldsymbol{q}_0)$ = gyroscopic damping matrix in finite element equation
I_p = polar moment of inertia of blade cross section, Ak_A^2
k_A = polar radius of gyration of blade cross section
k_m = mass radius of gyration of blade cross section, $\sqrt{k_{m_1}^2 + k_{m_2}^2}$
k_{m_1}, k_{m_2} = principal mass radii of gyration of blade cross section
$M(\boldsymbol{q}_0)$ = mass matrix in finite element equation
M_∞ = Mach number
m_0 = blade reference mass per unit length
N_b = number of blades
$\boldsymbol{n}$ = unit outward normal vector on the lifting blade surface
$\boldsymbol{P}(\boldsymbol{q}_0)$ = internal elastic load vector in finite element equation
$\boldsymbol{P}_A(\boldsymbol{q}_0)$ = generalized aerodynamic load vector in finite element equation
$\boldsymbol{P}_C(\boldsymbol{q}_0)$ = centrifugal load vector in finite element equation
$\tilde{\boldsymbol{q}}(t)$ = small perturbation about steady equilibrium position $\boldsymbol{q}_0$
$\boldsymbol{q}_0$ = generalized nodal displacement vector at steady equilibrium
R = blade radius
$T(x_1)$ = transformation matrix between undeformed and deformed blades
u_1, u_2, u_3 = components of displacement vector $\boldsymbol{u}$
$\boldsymbol{V}$ = local velocity of the blade surface
$\boldsymbol{W}$ = induced velocity because of all wake vortices
x_1, x_2, x_3 = blade curvilinear coordinates
$\alpha_1, \alpha_2, \alpha_3$ = orientation angles between undeformed and deformed blades in the order lead-lag, flap, and pitch angles
β_{pc} = blade precone angle
Γ = bound vortex strength
γ = Lock number, $3a_0\rho_a cR/m_0$
θ_p = blade collective pitch angle
ρ_a = air density
σ = blade solidity, $N_b c/\pi R$
ς = amplitude of torsional warping
ψ = dimensionless time, Ωt
Ω = rotor blade angular velocity
$\omega_F, \omega_L, \omega_T$ = nondimensional fundamental coupled rotating flap, lead-lag, and torsion frequencies, respectively

Introduction

MOST of the coupled flap-lag-torsion aeroelastic stability analyses of hingeless rotor blades in hover have been performed using the classical two-dimensional aerodynamic strip theory with a uniform induced inflow.[1–3] Two-dimensional aerodynamics used in these studies can predict neither the three-dimensional aerodynamic tip-relief nor the unsteady wake dynamics effects, which are very important in predicting the aerodynamic damping.

In recent years, however, three-dimensional unsteady aerodynamic models, such as the panel method[4] and the vortex lattice method,[5] with a prescribed wake geometry have successfully been applied to the aeroelastic response and stability of hingeless rotor blades. The generalized dynamic inflow model[6] including a three-dimensional shed wake inflow has also been used to evaluate the aerodynamic loads. In these analyses, the correlation studies with the experimental results of a small-scale hingeless rotor in hover[7] represent an improved prediction of the lead-lag damping values over the full range of collective pitch angles. The theoretical results in these

Received March 26, 1994; revision received Jan. 17, 1997; accepted for publication Jan. 23, 1997.

*Postdoctoral Fellow, Department of Aerospace Engineering, 373-1 Kusong-dong, Yusong-gu.
†Graduate Research Assistant, Department of Aerospace Engineering, 373-1 Kusong-dong, Yusong-gu.
‡Graduate Student, Department of Aerospace Engineering, 373-1 Kusong-dong, Yusong-gu.
§Professor, Department of Aerospace Engineering, 373-1 Kusong-dong, Yusong-gu. Member AIAA.

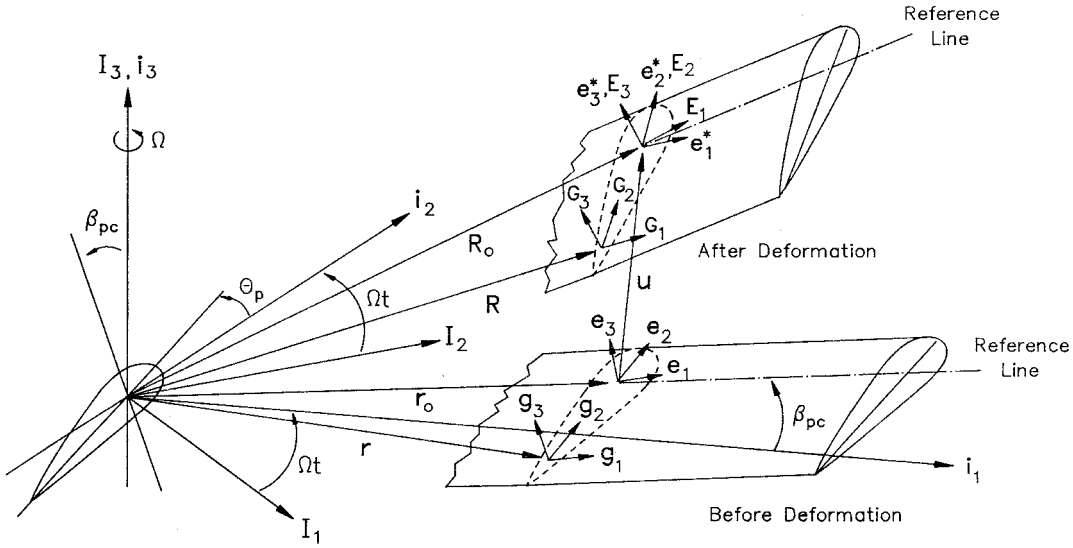

Fig. 1 Geometry and coordinate systems of a rotor blade before and after deformation.

studies were obtained by combining the unsteady airloads with conventional moderate deflection-type beam theories[8,9] based on the ordering scheme that limits the magnitude of blade displacements and rotations. The nonlinear aeroelastic equations of motion were formulated by Galerkin's method using the coupled rotating mode shapes of a beam.

Recently, a remarkable progress has been made in the structural models of rotor blades such as large deflection-type beam theories[10–12] not based on the ordering scheme. There are no small-angle approximations made and all kinematical nonlinear effects are included in these refined models. The aeroelastic analyses based on these structural models have also been performed.[13–17] Aeroelastic stability boundaries and steady tip deflections based on these theories are reported to be quite different from those based on moderate deflection-type beam theories when the collective pitch angle becomes large.[15–17] However, the aerodynamic model considered in these analyses was the two-dimensional quasisteady strip theory.

To perform the more reliable analysis in the rotor aeroelastic stability, the use of advanced rotary-wing aerodynamics with a sophisticated structural model is required since the aeroelastic stability is inherently a nonlinear phenomenon that involves structural, inertial, and aerodynamic loads. Thus, the refined structural model and the three-dimensional aerodynamics are used in this paper. The structural model used in the present analysis is based on Bauchau and Hong's finite element model.[10] The only assumption is that the strain is small compared with unity. This approach combined with an implicit formulation completely eliminates the need for using the ordering scheme. Transverse shearing deformations and torsional warping effects are included in the formulation. The present three-dimensional aerodynamic model is a thin lifting-surface theory based on the unsteady vortex lattice method.[18] A thin lifting-surface and its wake are represented by a number of quadrilateral vortex-ring elements, and the wake geometry is prescribed from the known generalized equations.[19,20] Compressibility effect is also considered. This compressibility effect gives quite significant results in the aerodynamic and aeroelastic analyses. The present method can predict the unsteady airloads of multibladed rotors and the effect of the interblade unsteady wake dynamics beneath the rotor blades on the aeroelastic response.

The finite element equations of motion are solved for the nonlinear steady deformation using the Newton–Raphson method. Assuming blade motions to be small perturbations about steady equilibrium positions, the aeroelastic response is calculated by a time-marching solution procedure, and then the stability analysis is performed by using a moving block analysis. The steady deflections and the stability have been investigated for cantilevered isotropic rotor blades with uniform section properties. The results are compared with those obtained by the two-dimensional quasisteady strip theory.

Blade Structural Model

Consider the rotor blade rotating with constant Ω depicted in Fig. 1. Here the triad $\boldsymbol{I}_1, \boldsymbol{I}_2, \boldsymbol{I}_3$ is fixed in an inertial frame and the triad $\boldsymbol{i}_1, \boldsymbol{i}_2, \boldsymbol{i}_3$ fixed in a reference frame that rotates with respect to the inertial frame at a constant angular velocity $\Omega \boldsymbol{I}_3$, and the triad $\boldsymbol{e}_1, \boldsymbol{e}_2, \boldsymbol{e}_3$ attached to a reference line along the axis of the undeformed blade. The curvilinear coordinates along this triad are x_1, x_2, and x_3, respectively. $\boldsymbol{e}_i$ and $\boldsymbol{E}_i$ (i = 1, 2, 3) are the base vectors at the positions $\boldsymbol{r}_0(x_1, 0, 0)$ and $\boldsymbol{R}_0(x_1, 0, 0)$ of the reference line, and $\boldsymbol{g}_i$ and $\boldsymbol{G}_i$ are the base vectors at the positions $\boldsymbol{r}$ and $\boldsymbol{R}$ of an arbitrary point of the cross section in the undeformed and deformed blade configurations, respectively. $\boldsymbol{e}_i^*$ is the new orthonormal triad at the reference line after deformation. Assuming that the initial curvatures are small and the axial and shearing strains are much smaller than unity in the Green–Lagrangian strain components (for more details see Ref. 10), the engineering strain components ε_{11}, γ_{12}, and γ_{13} are expressed as follows:

$$\varepsilon_{11} = \bar{e}_{11} - x_2\kappa_3 + x_3\kappa_2 + \lambda\varsigma' + k_1\left(x_3\frac{\partial\lambda}{\partial x_2} - x_2\frac{\partial\lambda}{\partial x_3}\right)\varsigma + \frac{1}{2}(2\bar{e}_{12} - x_3\kappa_1)^2 + \frac{1}{2}(2\bar{e}_{13} + x_2\kappa_1)^2 \tag{1}$$

$$\gamma_{12} = 2\bar{e}_{12} - x_3\kappa_1 + \frac{\partial\lambda}{\partial x_2}\varsigma, \qquad \gamma_{13} = 2\bar{e}_{13} + x_2\kappa_1 + \frac{\partial\lambda}{\partial x_3}\varsigma$$

where $\lambda(x_2, x_3)$ is the Saint Venant warping function, $\varsigma(x_1)$ is the warping amplitude, and $(\,)'$ means the derivative with respect to x_1. The force strains ($\bar{e}_{11}$, $2\bar{e}_{12}$, $2\bar{e}_{13}$) and moment strains (κ_1, κ_2, κ_3) components are given by

$$\begin{Bmatrix} \bar{e}_{11} \\ 2\bar{e}_{12} \\ 2\bar{e}_{13} \end{Bmatrix} = T(x_1)\begin{Bmatrix} u_1' + t_{11} \\ u_2' + t_{12} \\ u_3' + t_{13} \end{Bmatrix} - \begin{Bmatrix} 1 \\ 0 \\ 0 \end{Bmatrix} \tag{2}$$

$$\begin{Bmatrix} \kappa_1 \\ \kappa_2 \\ \kappa_3 \end{Bmatrix} = C_{k_1}\begin{Bmatrix} \alpha_1' \\ \alpha_2' \\ \alpha_3' \end{Bmatrix} - \begin{Bmatrix} k_1 \\ k_2 \\ k_3 \end{Bmatrix} \tag{3}$$

where

$$C_{k_1} = \begin{bmatrix} s_2 & 0 & 1 \\ c_2 s_3 & -c_3 & 0 \\ c_2 c_3 & s_3 & 0 \end{bmatrix}$$

where u_i are the components of the displacement vector $\boldsymbol{u}$ in the basic reference triad $\boldsymbol{i}_i$. The matrix T from the triad $\boldsymbol{i}_i$ to the triad $\boldsymbol{e}_i^*$ is defined as $\boldsymbol{e}_i^* = T_{ij}\boldsymbol{i}_j$. Here, $c_i = \cos\alpha_i$ and $s_i = \sin\alpha_i$; α_1, α_2, α_3 denote ψ (lead–lag angle), β (flap angle), and θ (pitch angle), respectively. t_{11}, t_{12}, t_{13} are the components of the transformation matrix from $\boldsymbol{i}_i$ to $\boldsymbol{e}_i$. k_1 is the pretwist, and k_2 and k_3 are initial curvatures of the blade.

The equations of motion for a hingeless isotropic rotor blade are obtained using Hamilton's principle. Additional details concerning strain energy and kinetic energy can be found in Ref. 17.

Three-Dimensional Aerodynamic Model

In the present analysis, rotor blades are regarded as thin lifting surfaces. These thin lifting surfaces and the wake region are discretized by a number of vortex-ring elements with piecewise constant strength (Fig. 2). In each panel of the blade surface, the leading segment of the vortex-ring is placed on the panel's quarter chord line and the collocation point is at the center of the three-quarter chord line. The boundary condition of no-flow penetration on the lifting surface should be satisfied at the collocation point of each panel where the Kutta condition is satisfied implicitly. Thus, the following algebraic equations, in terms of the unknown strength Γ of the bound vortex, can be obtained[18]:

$$[A]\{\Gamma\}_{\text{blade}} = \{\boldsymbol{V}\cdot\boldsymbol{n}\} - \{\boldsymbol{W}\cdot\boldsymbol{n}\}_{\text{wake}} \tag{4}$$

where $[A]$ is the unit strength bound vortex of each panel of the blade and $\boldsymbol{V}$ is the elastic motion and the rotation of the rotor blade. Here, $\{\boldsymbol{V}\cdot\boldsymbol{n}\}$ denotes the perpendicular component V_P of the velocity $\boldsymbol{V}$ with respect to the deformed blade coordinate system. Three components V_R (radial), V_T (tangential), and V_P of $\boldsymbol{V}$ are expressed as

$$\begin{Bmatrix} V_R \\ V_T \\ V_P \end{Bmatrix} = T\dot{u} + \begin{bmatrix} 0 & 0 & -x_2 \\ 0 & 0 & 0 \\ x_2 & 0 & 0 \end{bmatrix} C_{k_1}\dot{\alpha} + \Omega T \begin{bmatrix} 0 & -1 & 0 \\ 1 & 0 & 0 \\ 0 & 0 & 0 \end{bmatrix} \left(r_0 + u + T^T \begin{Bmatrix} 0 \\ x_2 \\ 0 \end{Bmatrix} \right) \tag{5}$$

where x_2 is the relative chordwise distance between the elastic axis and the collocation point of each panel and $(\dot{})$ denotes the time derivative. After obtaining Γ of each panel at each time step, the local pressure difference can be computed by using the unsteady Bernoulli equation. The resulting sectional unsteady lift, induced drag, and pitching moment are then obtained by adding the contribution of the individual chordwide panels.

Compressibility effect is considered by relating a pressure coefficient C_p with an incompressible pressure coefficient C_{p_0} at a given subsonic Mach number by the Prandtl–Glauert rule[21]:

$$C_p = C_{p_0}/\sqrt{1 - M_\infty^2} \tag{6}$$

Equation (6) relates an incompressible flow over a given two-dimensional profile to a subsonic compressible flow over the same profile.

In this analysis, the tip-vortex geometry is prescribed from the Kocurek and Tangler's recirculation model,[19] defining the axial and radial tip-vortex coordinates, and the geometry of the inboard wake sheet given by Landgrebe's wake model[20] is used. These wake geometries are functions of the rotor thrust coefficient, number of blades, collective pitch angle, and blade twist. Thus, the calculation of the steady loading is repeated until the converged solution of the whole vortex system is obtained for the given configuration parameters. As the linearized stability is performed in the present aeroelastic analysis, the unsteady loading is calculated for small perturbed motions of the blade about the steady equilibrium position.

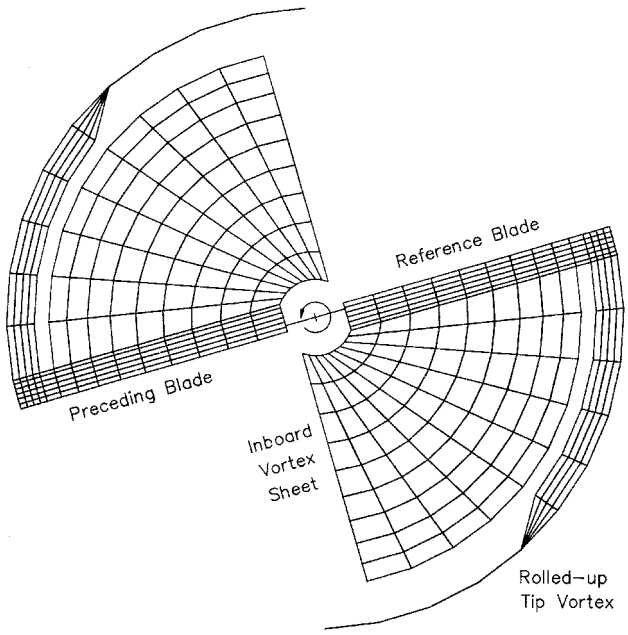

Fig. 2 Numerical lifting surface and wake vortex panels.

Solution Procedure

The finite element equations of motion for hingeless rotor blades can be formulated by using the Lagrangian elements with C^0 continuity as the shear deformation of the blade is allowed. Upon introducing the spatial discretization of the displacement u, the rotation α, and the warping amplitude ς into Hamilton's principle, the equations of motion in the matrix form are obtained:

$$[M(\boldsymbol{q})]\ddot{\boldsymbol{q}} + [G(\boldsymbol{q})]\dot{\boldsymbol{q}} + \boldsymbol{P}(\boldsymbol{q}) - \boldsymbol{P}_C(\boldsymbol{q}) = \boldsymbol{P}_A(t, \boldsymbol{q}) \tag{7}$$

where $[M]$ and $[G]$ are the mass and gyroscopic damping matrices in finite elements, respectively. $\boldsymbol{P}$ is the internal elastic force vector, $\boldsymbol{P}_C$ is the centrifugal force vector, $\boldsymbol{P}_A(t, \boldsymbol{q})$ is the generalized load vector because of the aerodynamic forces and pitching moment, and $\boldsymbol{q}$ is the generalized nodal displacement vector. To solve the governing equations of motion, the steady-state deformation because of steady aerodynamic loads and centrifugal forces is determined first. By dropping all time-dependent terms, the steady equilibrium equations are obtained: $\boldsymbol{P}(\boldsymbol{q}_0) - \boldsymbol{P}_C(\boldsymbol{q}_0) = \boldsymbol{P}_A(\boldsymbol{q}_0)$. The nonlinear steady deformation $\boldsymbol{q}_0$ is obtained through the iterative Newton–Raphson method. However, the linearization of Eq. (7) cannot be expressed in explicit form as in the two-dimensional aeroelastic analysis, since the aerodynamic forces and moment are complex nonlinear implicit functions of the blade deformation and motion at each instant of time. A direct eigenvalue analysis for determination of the stability is not possible. Thus, the linearized perturbation equations about the known equilibrium

deflections q_0 can be reduced to the first-order ordinary differential equations of the following form:

$$\begin{Bmatrix} \dot{\tilde{q}} \\ \ddot{\tilde{q}} \end{Bmatrix} = \begin{bmatrix} 0 & I \\ -M^{-1}K & -M^{-1}G \end{bmatrix} \begin{Bmatrix} \tilde{q} \\ \dot{\tilde{q}} \end{Bmatrix} + \begin{Bmatrix} 0 \\ M^{-1}\tilde{P}_A \end{Bmatrix} \tag{8}$$

where $K = K_T - K_C K_T$ and K_C are the tangent matrices for P and P_C, respectively. $\tilde{q}$ is the perturbed blade motion and $\tilde{P}_A$ the perturbed load vector which is calculated in real time base from the input of $\tilde{q}$. This system can be integrated numerically in time for the proper initial conditions of $\tilde{q}$, $\dot{\tilde{q}}$, and $\tilde{P}_A$. The initial value of $\tilde{q}$ is taken to be 10% of the equilibrium position q_0.[4] The time is set equal to zero at the initial perturbation and the blade is set free to move under the interaction of internal, inertial, and external aerodynamic loads. From the known values of the state vector and the perturbed aerodynamic loads, Eq. (8) is integrated by the fourth-order Runge–Kutta method. The position and orientation of the blade surface change from one time step to the next, and therefore [A] should be recomputed at every time step. In this analysis, the coefficient matrix, however, is computed only once for the steady equilibrium shapes of the deformed blade and the wake, because the unsteady motion of the blade is very small under the present small perturbation assumption, while the normal boundary condition is updated at each time step. To obtain more accurate modal damping and frequency, the initial perturbation of the blade is given only in the particular mode of interest. Once the time histories of the blade lead–lag, flap, and torsional deflections are known, the modal damping and frequency of any desired mode can be determined from the moving-block analysis.[22]

Discussion of Results

The numerical vortex-ring models of the blade surface and its wake for a two-bladed rotor considered in this analysis are presented in Fig. 2. The blade has an untwisted rectangular blade shape with 10% root cutout. The lifting surface is discretized by 6 (chordwise) × 14 (spanwise) vortex-ring elements. The dimensionless time step $\Delta\psi$ is 10 deg and the position of the rolled-up tip-vortex is 60 deg. The wake is considered up to two revolutions of the reference blade for the two-bladed rotor. To verify the present vortex lattice method (VLM), it was applied to a two-bladed rigid rotor. The blade has a solidity of 0.1061 with NACA 0012 airfoil section. The spanwise distribution of the normalized thrust loading for a rigid rotor is compared with the experimental[23] and panel method's results[4] in Fig. 3. The present VLM gives accurate results, including the three-dimensional tip-loss effect outside of the maximum sectional loading.

The three-dimensional tip-relief and unsteady wake dynamics effects for the two-bladed rigid rotor with AR = 10.3 are investigated. The normalized steady lift distribution at 10-deg collective pitch angle is shown in Fig. 4. The results are also compared with those obtained from the two-dimensional strip theory. The induced inflow in the strip theory is taken to be steady and uniform along the blade span and equal to the value of nonuniform inflow given by combined momentum/blade element theory at the 75% spanwise station. The result of the present VLM clearly represents the three-dimensional tip-loss effect that cannot be predicted using the strip theory and the uniform inflow distribution. Figure 5 presents the time histories of the perturbed lift for the hovering rotor undergoing a rigid pitching perturbation, $\Delta\theta_p = 0.1$ deg cos ωt, at 10-deg collective pitch angle. Here the dimensionless time step is taken to be 5 deg. There are transient peaks because of the starting vortex at earlier time steps. The results for the collective and differential modes do not show a clear difference until the wake vortices shed from the preceding blade approach the reference blade (half-revolution, 180 deg). After one revolution, there is a major difference in the perturbed lift because of the unsteady wake beneath the rotor. When the wake vortices shed from the preceding blade pass below the reference blade in the collective mode, the shed vortices make the induced inflow out-of-phase at $\omega/\Omega = 1$ and in-phase at $\omega/\Omega = 2$. This mechanism is reversed in the differential mode. Thus, the loading of the collective mode becomes higher ($\omega/\Omega = 1$ case) and smaller ($\omega/\Omega = 2$ case) than that of the differential mode, respectively. Figure 6 shows the spanwise incremental lift distribution at its maximum peak depicted in Fig. 5. Figure 6 indicates that the two-dimensional quasisteady aerodynamics lacks the tip-relief effect and does not predict the effect of unsteady inflow because of shed vorticity.

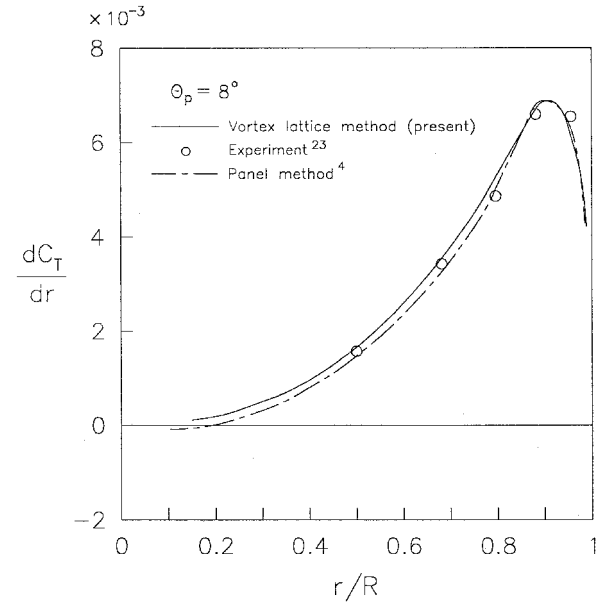

Fig. 3 Spanwise thrust loading of a two-bladed rigid rotor (AR = 6).

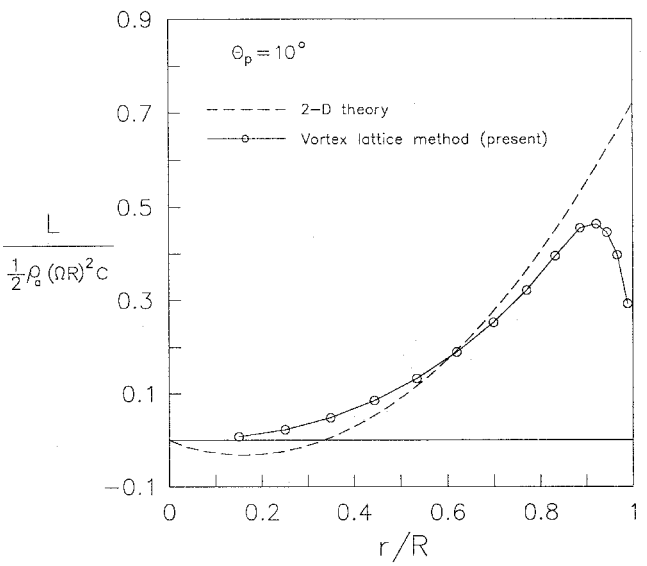

Fig. 4 Spanwise lift distribution of a two-bladed rigid rotor (AR = 10.3).

In the present aeroelastic analysis, the chordwise offsets of the c.m., tension center, and aerodynamic center from the elastic axis are considered to be zero. Assuming that the cross section is doubly symmetric, the present beam model is formulated by I_p (polar moment of inertia) for the torsional twist angle and D (section warping integral defined in Ref. 24) for the warping amplitude. Thus, to consider the warping deformation, a small value of D corresponding to 0.1% of I_p is used,

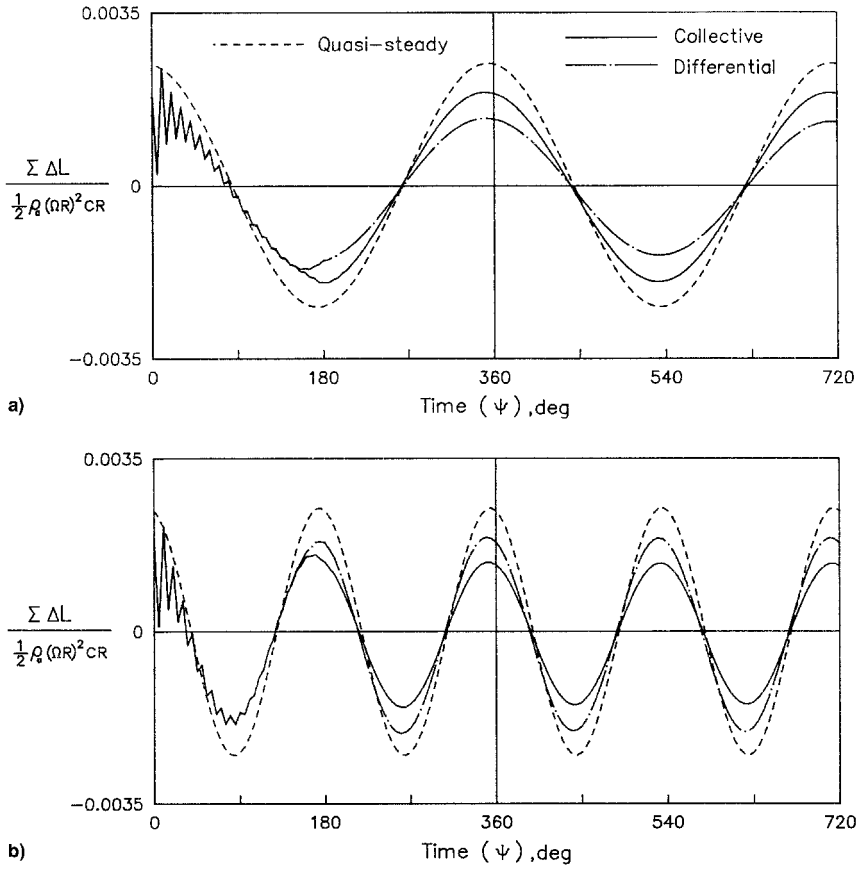

Fig. 5 Time histories of the perturbed lift at 10-deg collective pitch angle. Perturbed pitching motion, $\Delta\theta_p$ = 0.1 deg cos ωt with a) ω/Ω = 1 and b) ω/Ω = 2.

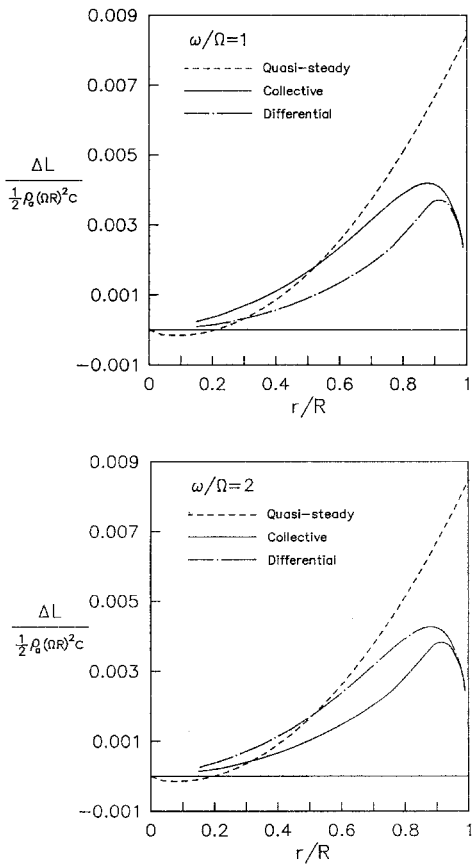

Fig. 6 Spanwise incremental lift distribution at its maximum peak.

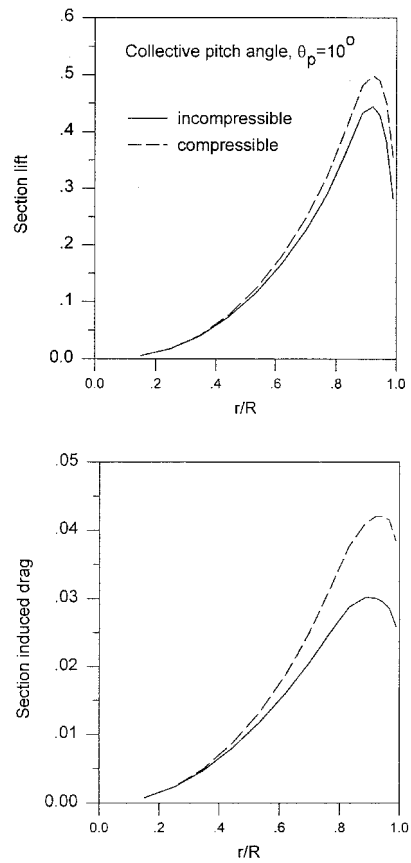

Fig. 7 Spanwise lift and induced drag distribution of two-bladed rotor at 10-deg collective pitch angle.

but the other section integrals including the warping are taken to be zero as in Refs. 1 and 3. The following common parameters (configurations and operating condition parameters) are used in the calculations:

$$k_m = 0.02778, \quad k_{m_1}/k_{m_2} = 0.0, \quad (k_A/k_m)^2 = 1.0, \quad \gamma = 6.308$$
$$\sigma = 0.06189, \quad N_b = 2, \quad c/R = 0.09722, \quad a_0 = 2\pi \qquad (9)$$
$$c_{d_0} = 0.01, \quad \beta_{pc} = 0, \quad (M_\infty)_{\text{tip}} = 0.7$$

The nondimensional rotating flap (ω_F), lead–lag (ω_L), and torsional (ω_T) frequencies used in the present calculations are 1.14, 1.3, and 3.0, respectively.

Figure 7 shows the sectional lift and the section-induced drag considering the compressibility effect at 10-deg collective pitch angle. The compressibility effect increases the sectional lift and the section-induced drag because the compressibility increases the C_p in Eq. (6). Figure 8 shows the normalized equilibrium flap, lead–lag, and torsion deflections at the blade tip. The tip flap deflections obtained from the two-dimensional theory are overestimated because of the higher thrust near the blade tip. The compressibility effect increases the tip flap deflections. The tip lead–lag deflections also show a similar trend. The tip torsional deflections predicted by the vortex lattice method are about one-third of those given by the two-dimensional theory. This is because of the three-dimensional tip effect that produces high nose-up pitching moment at the blade tip. The compressibility effect decreases the tip torsional deflections because the compressibility produces higher nose-up pitching moment. Figure 9 is the three-dimensional view of the undeformed and deformed blades and the wake region for the reference blade. Here, the position change of the vortex sheet because of the elastic deformation is considered up to the position of the rolled-up tip vortex (ψ = 60 deg), since the deformation is small compared with the whole wake region.

The time histories for blade motions obtained from an initial perturbation of the lead–lag mode are shown in Fig. 10. The results of the compressibility effect in the three-dimensional theory for two (collective and differential) dynamic modes are compared. The amplitudes of the two dynamic modes decreases more rapidly in the compressible case. The modal damping and frequency characteristics are determined through the moving-block analysis for the time histories. The lead–lag modal damping and frequency at various collective pitch angles are shown in Fig. 11. It is observed that the damping obtained from the three-dimensional method has a lower value than that from the quasisteady theory. The overprediction of lead–lag damping by the two-dimensional aerodynamics is be-

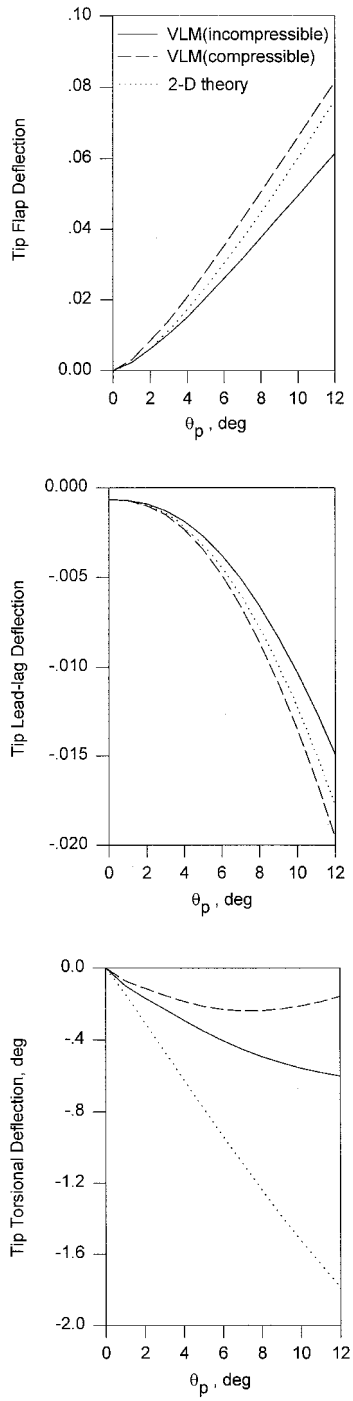

Fig. 8 Equilibrium tip deflections of two-bladed rotor at 10-deg collective pitch angle.

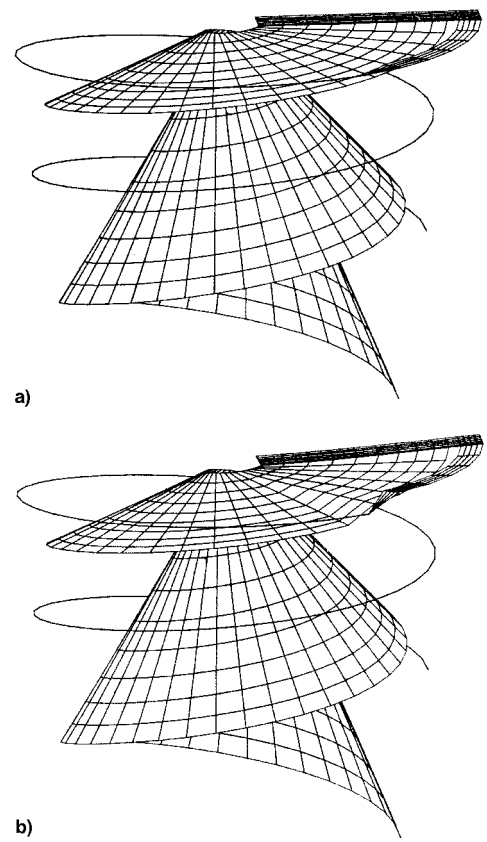

Fig. 9 Wake geometry of rigid and elastic blades at 12-deg collective pitch angle: a) rigid or undeformed blade and b) elastic or deformed blade.

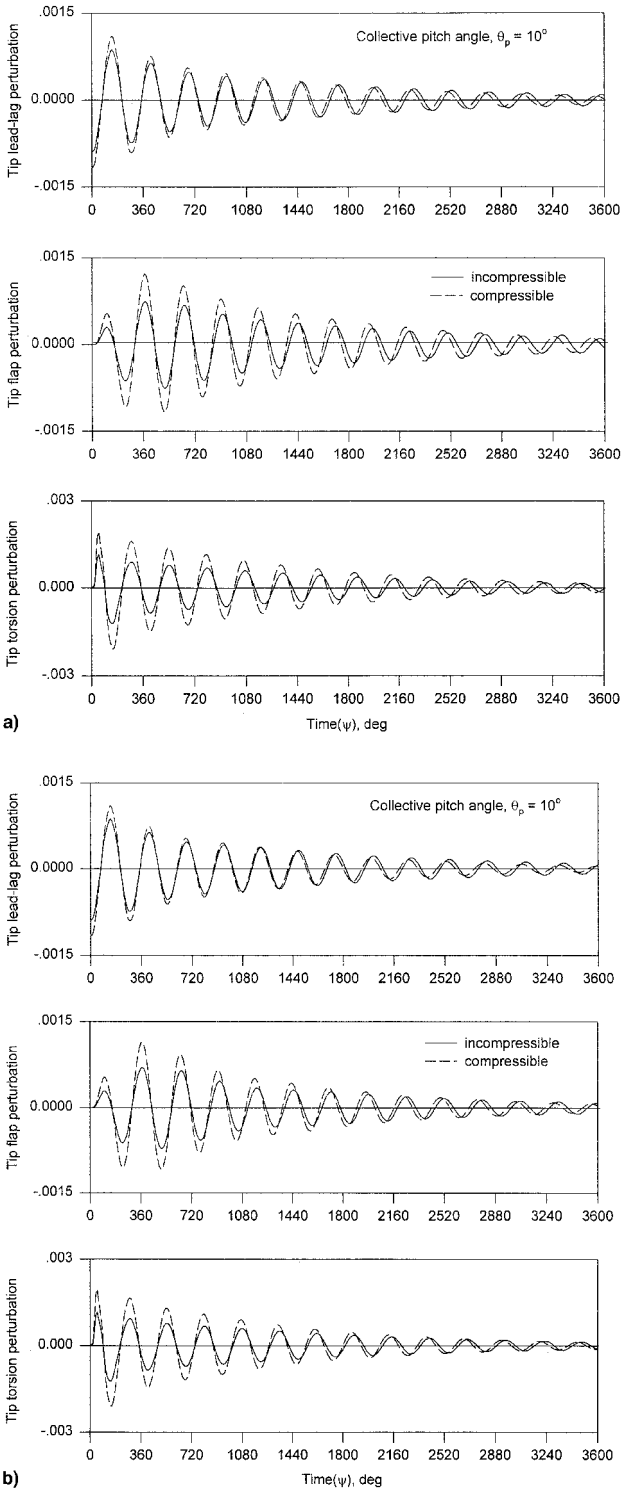

Fig. 10 Time histories of perturbed motions at 10-deg collective pitch angle obtained from an initial perturbation of lead–lag: a) collective and b) differential modes.

cause of a lack of both the three-dimensional tip-relief and unsteady wake dynamics effects. The compressibility effect increases the lead–lag damping. The lead–lag damping in the collective mode has slightly higher values than in the differential mode below about 9-deg collective pitch angle. The difference of the damping between collective and differential dynamic modes is because of the phase difference effect of vortices fluctuation as shown in Fig. 5. The lead–lag modal frequencies by the three aerodynamic models have a slight difference, but those are almost identical.

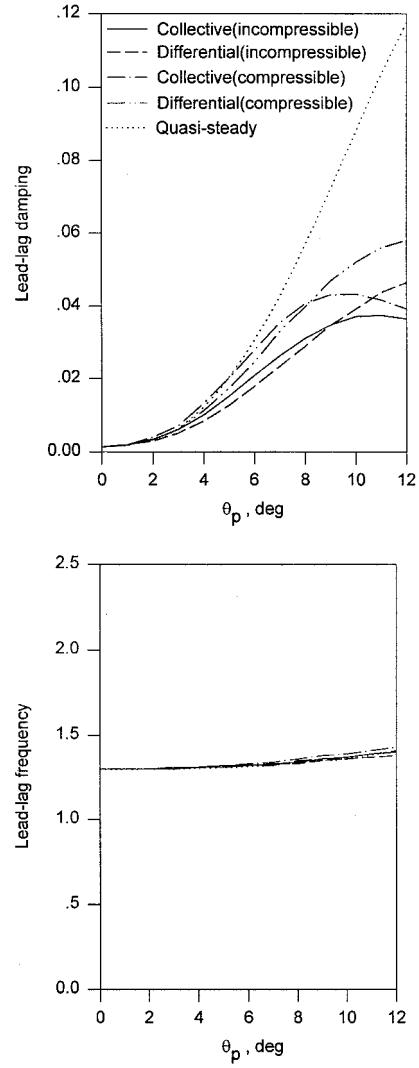

Fig. 11 Lead–lag damping and frequency of a stiff in-plane rotor.

Conclusions

In this paper the refined aeroelastic analysis of hingeless rotor blades in hover has been performed. The finite element formulation is obtained using the large deflection-type model that is not based on ordering scheme and includes all kinematic nonlinear effects. The unsteady vortex lattice method coupled with the prescribed wake geometry is used to evaluate the three-dimensional aerodynamic loads. The steady tip deflections and the lead–lag damping for a two-bladed stiff in-plane rotor are compared with those obtained by the two-dimensional quasisteady strip theory. The compressibility effect is also considered in the analyses. The results show that three-dimensional tip and realistic wake effects greatly affect the steady equilibrium and the rotor stability. Especially, the predicted torsional deflections are about one-third of those predicted by the two-dimensional theory. The lead–lag damping is predicted much smaller than that of the two-dimensional quasisteady theory. The compressibility effect increases the tip flap and lead–lag deflections because of the increase of the lift and induced drag and decreases the tip torsional deflections because of the increase of the nose-up pitching moment. The lead–lag damping is more conservative in the incompressible case. It is concluded that the three-dimensional aerodynamics should be used for the accurate prediction of the hingeless rotor stability in hover, since the two-dimensional aerodynamics cannot predict both the three-dimensional tip-relief and unsteady wake dynamics effects.

References

[1]Hodges, D. H., and Ormiston, R. A., "Stability of Elastic Bending and Torsion of Uniform Cantilever Rotor Blade in Hover with Variable Structural Coupling," NASA TN D-8192, April 1976.

[2]Friedmann, P. P., "Effect of Modified Aerodynamic Strip Theories on Rotor Blade Aeroelastic Stability," *AIAA Journal*, Vol. 15, No. 7, 1977, pp. 932–940.

[3]Sivaneri, N. T., and Chopra, I., "Dynamic Stability of a Rotor Blade Using Finite Element Analysis," *AIAA Journal*, Vol. 20, No. 5, 1982, pp. 716–723.

[4]Kwon, O. J., Hodges, D. H., and Sankar, L. N., "Stability of Hingeless Rotors in Hover Using Three-Dimensional Unsteady Aerodynamics, *Journal of the American Helicopter Society*, Vol. 36, No. 2, 1991, pp. 21–31.

[5]Yoo, K. M., Hodges, D. H., and Peters, D. A., "An Interactive Numerical Procedure for Rotor Aeroelastic Stability Analysis Using Lifting Surface," *Proceedings of the 18th ICAS Conference* (Beijing, PRC), 1992, pp. 1272–1280.

[6]De Andrade, D., and Peters, D. A., "Correlations of Experimental Flap-Lag-Torsion Damping — A Case Study," *Proceedings of the 49th Annual National Forum of the American Helicopter Society* (St. Louis, MO), American Helicopter Society, Alexandria, VA, 1993.

[7]Sharpe, D. L., "An Experimental Investigations of the Flap-Lag-Torsion Aeroelastic Stability of a Small-Scale Hingeless Helicopter Rotor in Hover," NASA TP-2546, Jan. 1986.

[8]Hodges, D. H., and Dowell, E. H., "Nonlinear Equations of Motion for Elastic Bending and Torsion of Twisted Non-Uniform Rotor Blades," NASA TN D-7818, Dec. 1974.

[9]Hodges, D. H., "Nonlinear Equations of Motion for Cantilever Rotor Blades in Hover with Pitch Link Flexibility, Twist, Precone, Droop, Sweep, Torque Offset, and Blade Root Offset," NASA TM X-73,112, May 1976.

[10]Bauchau, O. A., and Hong, C. H., "Nonlinear Composite Beam Theory," *Journal of Applied Mechanics*, Vol. 55, March 1988, pp. 156–163.

[11]Hodges, D. H., "A Mixed Variational Formulation Based on Exact Intrinsic Equations for Dynamics of Moving Beams," *International Journal of Solids and Structures*, Vol. 26, No. 11, 1990, pp. 1253–1273.

[12]Atilgan, A. R., and Hodges, D. H., "Unified Nonlinear Analysis for Nonhomogeneous Anisotropic Beams with Closed Cross Sections," *AIAA Journal*, Vol. 29, No. 11, 1991, pp. 1990–1999.

[13]Hodges, D. H., "Nonlinear Equations for the Dynamics of Pretwisted Beams Undergoing Small Strains and Large Rotations," NASA TP-2470, May 1985.

[14]Hodges, D. H., Hopkins, A. S., Kunz, D. L., and Hinnant, H. E., "Introduction to GRASP — General Rotorcraft Aeromechanical Stability Program — A Modern Approach to Rotorcraft Modeling," *Journal of the American Helicopter Society*, Vol. 32, No. 2, 1987, pp. 78–90.

[15]Fulton, M. V., and Hodges, D. H., "Aeroelastic Stability of Composite Hingeless Rotor Blades in Hover — Part I: Theory," *Mathematical and Computer Modelling*, Vol. 18, No. 3/4, 1993, pp. 1–18.

[16]Fulton, M. V., and Hodges, D. H., "Aeroelastic Stability of Composite Hingeless Rotor Blades in Hover — Part II: Results," *Mathematical and Computer Modelling*, Vol. 18, No. 3/4, 1993, pp. 19–36.

[17]Cho, M. H., and Lee, I., "Aeroelastic Stability of Hingeless Rotor Blade in Hover Using Large Deflection Theory," *AIAA Journal*, Vol. 32, No. 7, 1994, pp. 1472–1477.

[18]Kats, J., and Plotkin, A., *Low Speed Aerodynamics — From Wing Theory to Panel Method*, McGraw–Hill, New York, 1991, pp. 479–495.

[19]Kocurek, J. D., and Tangler, J. L., "A Prescribed Wake Lifting Surface Hover Performance Analysis," *Journal of the American Helicopter Society*, Vol. 22, No. 1, 1977, pp. 24–35.

[20]Landgrebe, A. J., "The Wake Geometry of a Hovering Helicopter Rotor and Its Influence on Rotor Performance," *Journal of the American Helicopter Society*, Vol. 17, No. 4, 1972, pp. 3–15.

[21]Anderson, J. D., "Linearized Flow," *Modern Compressible Flow*, 2nd ed., McGraw–Hill, New York, 1990, pp. 251–293.

[22]Hammond, C. E., and Doggett, R. V., Jr., "Determination of Subcritical Damping by Moving-Block/Randomdec Application," NASA Symposium on Flutter Testing Techniques, Oct. 1975.

[23]Caradona, F. X., and Tung, C., "Experimental and Analytical Studies of a Helicopter Rotor in Hover," NASA TM-81232, 1981.

[24]Hodges, D. H., "Torsion of Pretwisted Beam Due to Axial Loading," *Journal of Applied Mechanics*, Vol. 47, June 1980, pp. 393–397.